Raman scattering from antiferromagnetic spin fluctuations

Arno P. Kampf[1], **Wolfram Brenig**[2]

[1] Institut für Festkörperforschung Forschungszentrum Jülich, W-5170 Jülich, Federal Republic of Germany
[2] Institut für Theoretische Physik, Universität zu Köln, Zülpicher Strasse 77, W-5000 Köln 41, Federal Republic of Germany

A microscopic theory for the scattering of light from spin fluctuation pair modes in the two-dimensional Hubbard model is presented. Two-spin fluctuation processes with opposite momenta near the antiferromagnetic wave vector $\mathbf{Q}=(\pi,\pi)$ are shown to contribute in particular to the low energy part of the Raman cross section. We explicitly investigate the influence of the Raman vertex function that describes the coupling of the light to the electrons and distinguishes between the different scattering geometries. In addition we explore the dependence on the correlation strength and on the temperature.

I. Introduction

Electronic Raman scattering on nearly free electron metals is usually an effect of minor relevance. At typical wave vectors of the incident light the cross section is determined by the spectral intensity of the correlation function of density fluctuations which vanishes at small momentum transfer due to particle number conservation [1]. Moreover the window for inelastic frequency shifts is extremely narrow in the small wave vector regime. The discovery of pronounced Raman scattering on electronic excitations in the new high temperature superconductors is therefore of great interest and supports the importance of strong electronic correlations in these materials. It has revealed numerous unexpected features which still remain controversial. In particular a broad continuum of scattered intensity is found which extends from low energies of the order of $k_B T$ up to energies of approximately 1 eV [2, 3]. At frequency shifts below $k_B T/\hbar$ and for selected polarization geometries, e.g. the A_{1g} symmetry, the cross section vanishes proportional to ω/T, indicating a decay rate of the relevant electronic excitations which is linear in temperature [3]. These findings have stimulated speculations on a 'marginal' behavior of a possible Fermi liquid underlying the normal state of the high temperature superconductors [4], but have also been described within more conventional schemes [5, 6].

Apart from these effects a different source of scattering exists which is particularly evident in the undoped parent compounds. These materials exhibit inelastic light scattering resonances at frequencies of the order of $3000\ldots4000\ \mathrm{cm}^{-1}$, e.g. in La_2CuO_4 and $YBa_2Cu_3O_{6.2}$ [2, 7], and somewhat weaker at approximately two times this value. The selection rules, the resonance position and the first non trivial moments of these features strongly support the concept of scattering from two and four magnon excitations of the two dimensional spin 1/2 Heisenberg antiferromagnet of copper spins [2, 3, 8] in the CuO_2 planes. Two-magnon Raman scattering is well established, experimentally as well as theoretically [9], in more conventional antiferromagnetic (AF) insulators with larger spin like Rb_2MnF_4 [10] with $S=5/2$ and K_2NiF_4 with $S=1$ [11]. A description of the scattering intensity in terms of electronic density fluctuations seems unlikely in these systems, since due to the vanishing electronic compressibility density fluctuations are strongly suppressed in the insulating regime. This also applies to the *doped* cuprates due to their immediate vicinity to the metal insulator transition as has been pointed out recently by Shastry and Shraiman [12]. In this work it was shown that light scattering from Mott-Hubbard systems close to half filling can be described by an effective scattering Hamiltonian which is equivalent to the Hamiltonian used by Elliott et al. [13]. The latter couples the electric field of the incident photon to a two-spin flip process and it was used to analyze magnetic Raman scattering in conventional antiferromagnets. This approach provides also a theoretical basis of Raman scattering on magnetic excitations in undoped cuprates.

Experimentally it is well established that spin fluctuations are not only relevant to the insulating AF phases of the layered cuprates but also lead to prominent low energy collective excitations in the doped materials. This is evident not only from neutron scattering data which exhibit appreciable spectral intensity close to the wave vector (π,π) indicating short range AF order even in

the superconducting compounds [14] but also from the deviations from Korringa's law for the temperature dependence of the copper NMR relaxation rate [15, 16]. At finite doping concentrations the two-magnon Raman feature is found to broaden and to shift to lower frequencies [17]. This is suggestive of a transition from sharp spin wave excitations to overdamped paramagnons. The polarization dependence of the scattering on these remnants of the two-spin resonance seems less crucial in doped systems. In particular the A_{1g} and B_{2g} channels, which contribute only very little to the Raman scattering in the AF compounds, develop finite intensity for finite doping concentrations. The relative contribution of magnetic scattering to the total Raman cross section, however, remains unclear.

All these phenomena raise the interest for a theoretical description of light scattering from spin fluctuations in itinerant systems close the magnetic instability. Previous work on this topic was mainly phenomenological [5]. In the present investigation we provide a microscopic treatment of the Raman scattering from two-magnon excitations in the two dimensional Hubbard model. The paper is organized as follows: in Sect. II we start with a review of the basic notions of electromagnetic response and the scattering of light as applied to the Hubbard model. Section III is devoted to the description of our diagrammatic approach and in Sect. IV we describe in detail the evaluation of the Raman vertex function and the dynamical spin susceptibility. A discussion of our results is presented in Sect. V, and finally we conclude in Sect. VI.

II. Electronic Raman scattering

We start from the Hubbard Hamiltonian on a square lattice in the presence of an external transverse electromagnetic photon field represented by the vector potential **A** in the usual Peierls description

$$H_{\mathbf{A}} = -t \sum_{\langle ij\rangle,\sigma} \left[\exp\left(i \frac{e}{\hbar c} \int_i^j \mathbf{A}\cdot\mathbf{dl} \right) c_{i\sigma}^{+} c_{j\sigma} + \text{h.c.} \right] + U \sum_i n_{i\uparrow} n_{i\downarrow} \tag{1}$$

$c_{i\sigma}^{+}(c_{i\sigma})$ destroys (creates) an electron of spin σ on the site i of the lattice and the sum on $\langle ij\rangle$ is restricted to nearest neighbors. t and U represent the hopping integral and the on-site Coulomb repulsion, respectively, and $n_{i\sigma}$ is the local density. Since the photon field is a weak perturbation we expand to second order in **A** and in performing the Fourier transformation we introduce the components of the current operator

$$j_{\mathbf{q}}^{\alpha} = \sum_{\mathbf{k},\sigma} \frac{\partial \varepsilon_{\mathbf{k}}}{\partial k_\alpha} c^{+}_{\mathbf{k}+\frac{\mathbf{q}}{2},\sigma} c_{\mathbf{k}-\frac{\mathbf{q}}{2},\sigma} \tag{2}$$

and the components of the 'inverse mass tensor'

$$\tau_{\mathbf{q}}^{\alpha\beta} = \sum_{\mathbf{k},\sigma} \frac{\partial^2 \varepsilon_{\mathbf{k}}}{\partial k_\alpha \partial k_\beta} c^{+}_{\mathbf{k}+\frac{\mathbf{q}}{2},\sigma} c_{\mathbf{k}-\frac{\mathbf{q}}{2},\sigma} \tag{3}$$

Table 1. Scattering geometries for different combinations of the polarisation vectors of the incoming and outgoing photons $\mathbf{e}_i$ and $\mathbf{e}_f$, respectively

Symmetry	$\mathbf{e}_i$	$\mathbf{e}_f$
A_{1g}	$\frac{1}{\sqrt{2}}(1,1)$	$\frac{1}{\sqrt{2}}(1,1)$
B_{1g}	$\frac{1}{\sqrt{2}}(1,1)$	$\frac{1}{\sqrt{2}}(1,-1)$
B_{2g}	$(1,0)$	$(0,1)$

with the tight binding dispersion $\varepsilon_{\mathbf{k}} = -2t(\cos(k_x a) + \cos(k_y a))$. For a free electron dispersion $\tau_{\mathbf{q}}^{\alpha\beta}$ is proportional to the familiar density operator. With this notation we obtain the effective Hamiltonian (in units where $\hbar = 1$)

$$H_{\mathbf{A}} = H_{\mathbf{A}=0} - \frac{e}{c} \sum_{\mathbf{q}\alpha} j_{\mathbf{q}}^{\alpha} A_{-\mathbf{q}}^{\alpha} + \frac{1}{2}\left(\frac{e}{c}\right)^2 \sum_{\mathbf{q}_1,\mathbf{q}_2,\alpha,\beta} \tau_{\mathbf{q}_1+\mathbf{q}_2}^{\alpha\beta} A_{-\mathbf{q}_1}^{\alpha} A_{-\mathbf{q}_2}^{\beta}. \tag{4}$$

In the second quantized form the components of the electromagnetic field operator A^{α} are given by

$$A_{\mathbf{q}}^{\alpha} = \sqrt{\frac{hc^2}{\omega_{\mathbf{q}} \Omega}} (e_\alpha a_{-\mathbf{q}} + \bar{e}_\alpha a_{\mathbf{q}}^{+}) \tag{5}$$

where e_α are the complex components of the unit vector **e** of the photon polarisation and the overbar denotes complex conjugation. The polarisation vectors for the commonly used experimental configurations (A_{1g}, B_{1g}, and B_{2g}) with linearly polarized light are collected in Table 1 following the notation of [18]. $\omega_{\mathbf{q}} = c|\mathbf{q}|$ is the photon energy and $a_{\mathbf{q}}^{+}$ ($a_{\mathbf{q}}$) are the photon creation (annihilation) operators, respectively.

The Raman scattering cross section is proportional to the transition rate R which can be obtained by applying Fermi's golden rule. The inelastic scattering rate for transitions with energy and momentum transfer $\Delta\omega = \omega_i - \omega_f$ and $\mathbf{q} = \mathbf{k_i} - \mathbf{k_f}$ is therefore of the form

$$R(\mathbf{q}, \Delta\omega) = \frac{2\pi c^2}{\Omega \sqrt{\omega_i \omega_f}} \left(\frac{e}{c}\right)^4 \sum_{i,f} \frac{e^{-\beta\varepsilon_i}}{Z} |\langle f|\hat{M}|i\rangle|^2 \cdot \delta(\varepsilon_i - \varepsilon_f - \Delta\omega) \tag{6}$$

Z is the partition function and $\beta = 1/k_B T$ is the inverse temperature. $\hat{M}$ is the effective Raman scattering operator responsible for transitions between initial and final eigenstates of the Hubbard Hamiltonian with energy eigenvalues ε_i and ε_f, respectively. From the electron-light coupling Eq.(4) there are two contributions to $\hat{M}$, a direct scattering from the coupling to the 'inverse mass tensor' and a resonant contribution from the coupling to the current, which involves virtual intermediate states of the correlated electron system. Explicitly one finds

$$\langle f|\hat{M}|i\rangle=\sum_{\alpha,\beta} e_i^{\alpha}\bar{e}_f^{\beta}\langle f|\tfrac{1}{2}\tau_{\mathbf{q}}^{\alpha\beta}+\hat{M}_R^{\alpha\beta}|i\rangle \tag{7a}$$

$$\langle f|\hat{M}_R^{\alpha\beta}|i\rangle = \sum_{\nu}\left[\frac{\langle f|j^{\beta}_{\mathbf{k}_f}|\nu\rangle\langle\nu|j^{\alpha}_{-\mathbf{k}_i}|i\rangle}{\varepsilon_\nu-\varepsilon_i-\omega_i}+\frac{\langle f|j^{\alpha}_{-\mathbf{k}_i}|\nu\rangle\langle\nu|j^{\beta}_{\mathbf{k}_f}|i\rangle}{\varepsilon_\nu-\varepsilon_i+\omega_f}\right] \tag{7b}$$

Eq. (7b) arise from two different time orderings. Using the fluctuation-dissipation theorem it is useful to rewrite the transition rate in terms of the imaginary part of the corresponding dynamical susceptibility,

$$R(\mathbf{q},\Delta\omega)=[1+n(\Delta\omega)]\cdot\frac{c^2}{\Omega\sqrt{\omega_i\omega_f}}\left(\frac{e}{c}\right)^4\int \mathrm{d}t\, e^{-i\Delta\omega t}\langle[\hat{M}^{+}(0),\hat{M}(t)]\rangle \tag{8}$$

Here, $n(\Delta\omega)=(e^{\beta\Delta\omega}-1)^{-1}$ is the Bose distribution function and we have rewritten the scattering operator as [12]

$$\hat{M}(t)=\sum_{\alpha\beta} e_i^{\alpha}\, e_f^{-\beta}\cdot\left(\frac{1}{2}\tau_{\mathbf{q}}^{\alpha\beta}(t)+i\int_0^{\infty}\mathrm{d}t'\,[j^{\alpha}_{-\mathbf{k}_i}(t+t'),j^{\beta}_{\mathbf{k}_f}(t)]\,e^{-i\omega_i t'}\right). \tag{9}$$

Since the wavelength of light in the optical range is large compared to the lattice spacing and all length scales of the electronic system, we can safely neglect the momentum transfer of the photon to the electrons and we will from now on use $\mathbf{q}=\mathbf{k}_i-\mathbf{k}_f=0$. Note that the derivation did not rely on any specific form of the electron-electron interaction since the photon field couples to the electrons only through the phase factor in the kinetic energy.

The result for the scattering operator shows that the general form of the Raman intensity involves density-density, four current and mixed current-density correlations. Equations (8) and (9) may serve as a starting point for a perturbative analysis, but in this form it is hard to disentangle specifically the contributions from AF spin fluctuations which dominate the dynamic response functions in the Hubbard model near half-filling. For this purpose it is useful to follow alternatively a diagrammatic approach which allows to single out the contributions we are interested in.

III. Raman scattering from spin fluctuations

A somewhat different route to the evaluation of the Raman intensity results from the well known fact, that the transition rate given in (6) can be obtained from the imaginary part of the fully dressed two-photon Green's function. In particular, given any specific subclass of diagrams which contribute to the two-photon Green's function, its imaginary part can be deduced from taking the so called *cuts* of all these diagrams. Choosing a specific subclass of diagrams and a selected set of cuts that leads to an expression in accordance with the golden rule is a nontrivial task. We will follow here the formalism of Kawabata [19] who applied the two-photon Green's function approach to the problem of Raman scattering from phonons. In this work a detailed description has been given for the cut procedure and the related selection of the relevant branches for the analytic continuation.

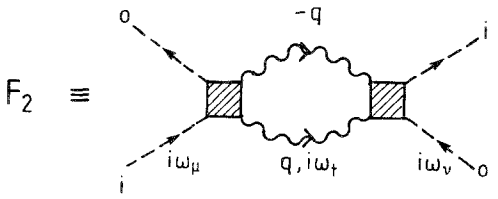

Fig. 1. General diagram for the Raman intensity from two-spin fluctuation scattering. The broken lines represent the incoming (i) and outgoing (o) photon and the wiggly line the propagator (susceptibility) for the spin fluctuation

We apply Kawabata's method and its extension to two-phonon Raman scattering [20] to the problem of Raman scattering from AF spin fluctuations. Since Raman scattering is a $\mathbf{q}=0$ probe an even number of AF fluctuations is necessary to satisfy the matching conditions with a momentum transfer close to the AF wave vector $\mathbf{Q}=(\pi,\pi)$ for *each* of the fluctuation propagators involved. Here, we will focus on Raman scattering from *two* spin fluctuations. Thus, the relevant contributions will arise from two-spin fluctuations with opposite momenta near $\mathbf{Q}$, as in the case of two-magnon scattering in ordered antiferromagents. This is represented by the general diagram in Fig. 1 where the light couples to the electronic system by means of a vertex function creating internally two spin fluctuations of momenta $\mathbf{q}$ and $-\mathbf{q}$, respectively. Following [19] and [20] we evaluate the diagram $\mathscr{F}_2$ in the finite temperature formalism and introduce three independent external frequencies as indicated in Fig. 1.

Given the vertex function $V_{\mathbf{q}}$ and the spin fluctuation propagator, i.e. the spin susceptibility, which will be evaluated both in Sect. IV, we have to calculate

$$\mathscr{F}_2(i\omega_\mu,i\omega_\nu,i\omega_t)=\frac{1}{\beta}\sum_{m\mathbf{q}} V_{\mathbf{q}}(i\omega_\mu,i\omega_t,i\omega_m)\,U^2\,\chi(\mathbf{q},i\omega_m+i\omega_t)\cdot U^2\,\chi(-\mathbf{q},-i\omega_m)\,V_{\mathbf{q}}(i\omega_\nu,-i\omega_t,-i\omega_m) \tag{10}$$

where the $i\omega_\mu$ are bosonic Matsubara frequencies. Here, for our convenience, we have split off factors of U^2 from the vertex function. The reason for this will become apparent in Chap. IV. In order to compute $\mathscr{F}_2$ we introduce the spectral representation for the spin susceptibility

$$\chi(\mathbf{q},i\omega_\nu)=-\int\frac{\mathrm{d}\omega'}{\pi}\frac{\mathrm{Im}\chi(\mathbf{q},\omega')}{i\omega_\nu-\omega'}. \tag{11}$$

In principle the frequency sum of (10) has to be performed taking into account all existing branch cuts, including those which result from the analytic structure of the vertex functions. Here, we include only the regular part of the vertex [20], i.e. we carry out the internal frequency sum excluding possible residue contributions

from the vertex function. The subsequent analytical continuation to real frequencies requires to identify [20]

$$i\omega_\mu \to \omega_i + i\delta \qquad i\omega_\nu \to -\omega_i + i\delta \qquad i\omega_t \to \Delta\omega \pm i\delta \tag{12}$$

where $\Delta\omega = \omega_i - \omega_f$ is the Raman frequency shift introduced earlier. Within the above approximation of a regular vertex function only one cut across the spin fluctuation lines in the diagram is needed to obtain the scattering intensity. This translates into taking the discontinuity of $\mathscr{F}_2$ across the real frequency axis with respect to $i\omega_t$, i.e.

$$\frac{1}{2\pi i}[\mathscr{F}_2(\omega_i + i\delta, -\omega_i + i\delta, \Delta\omega + i\delta) - \mathscr{F}_2(\omega_i + i\delta, -\omega_i + i\delta, \Delta\omega - i\delta)]. \tag{13}$$

This yields for the contribution from spin fluctuations to the total Raman scattering intensity

$$I(\Delta\omega, T) = (1 + n(\Delta\omega)) \sum_q \int d\omega' |V_{\mathbf{q}}(\omega_i + i\delta, \Delta\omega, \omega')|^2 \cdot (n(\omega') - n(\omega' - \Delta\omega)) \cdot U^2 \operatorname{Im}\chi(\mathbf{q}, \omega' + \Delta\omega)\, U^2 \operatorname{Im}\chi(-\mathbf{q}, \omega'). \tag{14}$$

This convolution of two spectral functions for the spin fluctuations has the expected form for a transition rate. The appearance of the absolute square of the vertex function is a consequence of the highly symmetric cut of the diagram. If the internal structure of the vertex, i.e. the residue contributions excluded above, is taken into account further possibilities arise for taking cuts providing additional contributions to the electronic Raman scattering. Here, however, we focus on the selected cut since we expect its contribution to be relevant in the presence of strong AF spin correlations.

IV. The vertex part and $\chi(\mathbf{q}, \omega)$

The evaluation of the scattering intensity $I(\Delta\omega, T)$ in (14) requires to provide two input quantities: the vertex function $V_{\mathbf{q}}$ and the spin susceptibility. The electron-photon Hamiltonian (4) already displayed the bare scattering vertices from the coupling to the current and to the density of the correlated electron system. From these two basic scattering vertices four different diagrams follow which add up to the total vertex function $V_{\mathbf{q}}$ shown in Fig. 2. Here, the diagrams (a), (b), and (c) directly reflect the explicit form of the scattering operator in (7). The contribution (d) from the rhomb shaped diagram, however, is equally valid and simply corresponds to another time ordering for the absorption (emission) of a photon and the creation of the internal excitation, i.e. the spin fluctuation. Yet, this diagram has not been included in similar diagrammatic approaches to electronic Raman scattering [20]. In our calculation, however, we find this diagram to be comparable in magnitude to the other three contributions and it is included in our subsequent analysis.

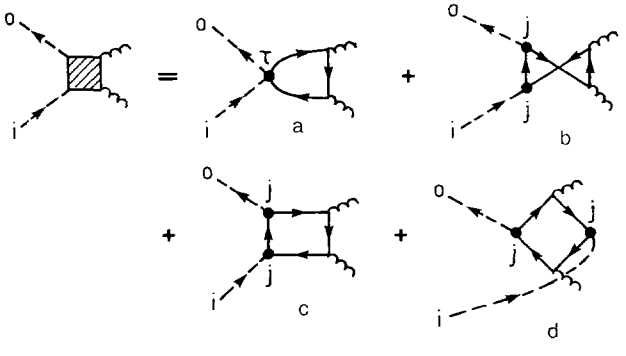

Fig. 2a–d. Four-vertex function for two-spin fluctuation Raman scattering from the coupling to the inverse mass **a** and the current operator **b, c** and **d** for different time orderings

For a given spin σ the vertex diagrams are given by

$$V_{\mathbf{q}}^{\tau}(i\omega_\mu, i\omega_t, i\omega_m) = -\frac{1}{\beta}\sum_{\mathbf{k},n} M_\tau(\mathbf{k})\, G_0^\sigma(\mathbf{k}, i\Omega_n) \cdot G_0^\sigma(\mathbf{k}, i\Omega_n + i\omega_t)\, G_0^\sigma(\mathbf{k}-\mathbf{q}, i\Omega_n - i\omega_m) \tag{15a}$$

$$V_{\mathbf{q}}^{j}(i\omega_\mu, i\omega_t, i\omega_m) = -\frac{1}{\beta}\sum_{\mathbf{k},n} M_j(\mathbf{k})\, G_0^\sigma(\mathbf{k}, i\Omega_n) \cdot G_0^\sigma(\mathbf{k}, i\Omega_n + i\omega_\mu)\, G_0^\sigma(\mathbf{k}, i\Omega_n + i\omega_t) \cdot [G_0^\sigma(\mathbf{k}-\mathbf{q}, i\Omega_n - i\omega_m) + G_0^\sigma(\mathbf{k}-\mathbf{q}, i\Omega_n + i\omega_m + i\omega_t)] \tag{15b}$$

$$V_{\mathbf{q}}^{r}(i\omega_\mu, i\omega_t, i\omega_m) = -\frac{1}{\beta}\sum_{\mathbf{k},n} M_r(\mathbf{k}, \mathbf{q})\, G_0^\sigma(\mathbf{k}, i\Omega_n) \cdot G_0^\sigma(\mathbf{k}, i\Omega_n + i\omega_\mu)\, G_0^\sigma(\mathbf{k}, i\Omega_n + i\omega_m + i\omega_\mu) \cdot G_0^\sigma(\mathbf{k}+\mathbf{q}, i\Omega_n + i\omega_m + i\omega_t). \tag{15c}$$

The total vertex function is obtained from the sum $V_{\mathbf{q}} = V_{\mathbf{q}}^{\tau} + V_{\mathbf{q}}^{j} + V_{\mathbf{q}}^{r}$. For the fermion lines undressed free particle propagators for the tight binding band of the square lattice are used, i.e. $G_0^\sigma(\mathbf{k}, i\Omega_n) = (i\Omega_n - \varepsilon_{\mathbf{k}})^{-1}$ with the fermionic Matsubara frequencies $i\Omega_n = i(2n+1)\pi/\beta$. The symmetry of the basic scattering vertices has been combined into the factors M_τ, M_j, and M_r together with the components of the photon polarisation vectors. It is these symmetry factors of the vertex function which distinguish between the different scattering geometries. They follow from

$$M_\tau(\mathbf{k}) = \frac{\pi e^2}{\Omega\sqrt{\omega_i \omega_f}} \sum_{\alpha\beta} \frac{\partial^2 \varepsilon_{\mathbf{k}}}{\partial k_\alpha \partial k_\beta} e^\alpha \bar{e}^\beta \tag{16a}$$

$$M_r(\mathbf{k}, \mathbf{q}) = \frac{2\pi e^2}{\Omega\sqrt{\omega_i \omega_f}} \sum_{\alpha\beta} \frac{\partial \varepsilon_{\mathbf{k}}}{\partial k_\alpha} \frac{\partial \varepsilon_{\mathbf{k}+\mathbf{q}}}{\partial k_\beta} e^\alpha \bar{e}^\beta \tag{16b}$$

$$M_j(\mathbf{k}) = M_r(\mathbf{k}, \mathbf{q}=0). \tag{16c}$$

The explicit results for the A_{1g}, B_{1g}, and B_{2g} scattering geometries are collected in Table 2. We may add that the diagrammatic representation for the vertex function also allows an extension to a multiband situation when the dependence of $V_{\mathbf{q}}$ on the incoming light frequency gives rise to resonant effects from interband transitions.

For the calculation of the spin susceptibility we apply the weak coupling RPA approximation and sum the standard ladder and bubble diagrams for the Hubbard

Table 2. Symmetry coefficients of the vertex function for different scattering geometries. The coefficients M_α introduced in (15) with $\alpha \in \{\tau, r, j\}$ are related to the quantities P_α listed in the table by $M_\alpha = \frac{\pi e^2}{\Omega \sqrt{\omega_i \omega_f}} P_\alpha$

	$P_\tau(\mathbf{k})$	$P_r(\mathbf{k}, \mathbf{q})$	$P_j(\mathbf{k})$
A_{1g}	$\cos k_x + \cos k_y$	$4(\sin k_x + \sin k_y)(\sin(k_x+q_x) + \sin(k_y+q_y))$	$4(\sin k_x + \sin k_y)^2$
B_{1g}	$\cos k_x - \cos k_y$	$4(\sin k_x + \sin k_y)(\sin(k_x+q_x) - \sin(k_y+q_y))$	$4(\sin k_x - \sin k_y)^2$
B_{2g}	0	$8 \sin k_x \sin(k_y+q_y)$	$8 \sin k_x \sin k_y$

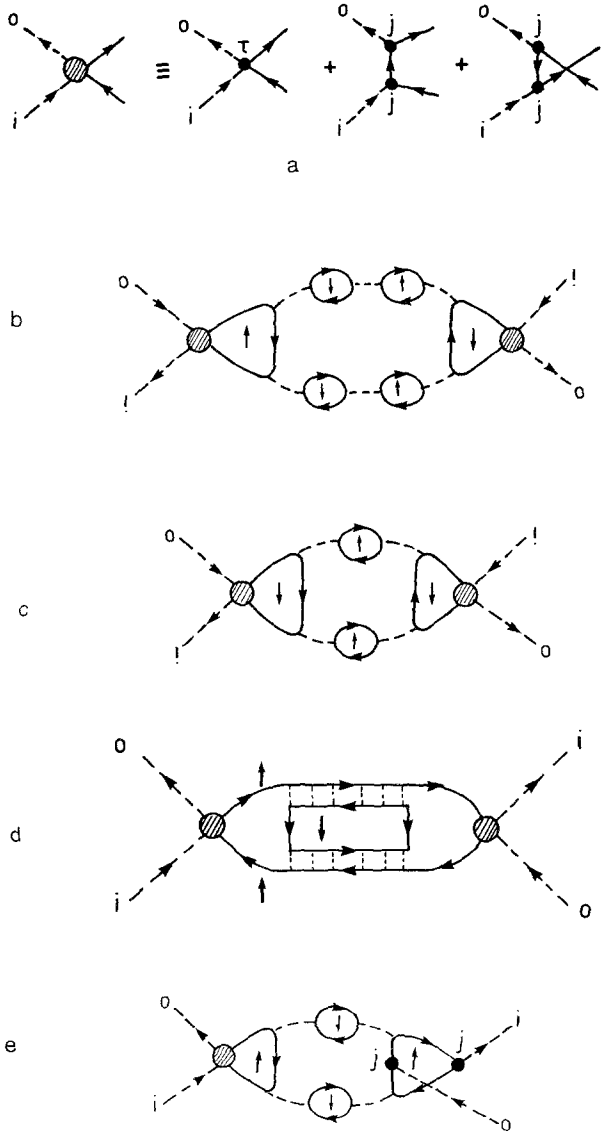

Fig. 3. a Effective vertex used in **b–d** (Note that these elementary photon-electron scattering vertices also appear as part of the vertex function in Fig. 2. **b–d** show the lowest order diagrams which are summed in the RPA series for the susceptibility, separated into **b** the 'even bubble', **c** the 'odd bubble', and **d** the ladder contributions. **e** Example for an 'odd bubble' diagram which involves the rhomb part of the vertex. These diagrams are included in the calculation, but they are not simply represented by using the effective vertex introduced in **a**

model [21]. The different lowest order contributions are shown in Fig. 3. Spin constraints impose an even (odd) number of closed particle hole loops or elementary bubbles between the fermion lines of opposite (parallel) spin which are part of the vertex. We therefore have to consider separatly the contributions $\chi^{\uparrow\downarrow}$ and $\chi^{\uparrow\uparrow} = \chi^{\downarrow\downarrow}$ leading to

$$U^2 \chi^{\uparrow\downarrow}(\mathbf{q}, \omega) = U + \frac{U^2 \chi_0(\mathbf{q}, \omega)}{1 - U \chi_0(\mathbf{q}, \omega)} + \frac{U^3 \chi_0^2(\mathbf{q}, \omega)}{1 - U^2 \chi_0^2(\mathbf{q}, \omega)} \quad (17a)$$

$$U^2 \chi^{\uparrow\uparrow}(\mathbf{q}, \omega) = -\frac{U^2 \chi_0(\mathbf{q}, \omega)}{1 - U^2 \chi_0^2(\mathbf{q}, \omega)}. \quad (17b)$$

The elementary bubble $\chi_0(\mathbf{q}, \omega)$ is the susceptibility of the noninteracting system ($U = 0$) as given by the Lindhard function

$$\chi_0(\mathbf{q}, \omega) = \frac{1}{N} \sum_p \frac{f(\varepsilon_{\mathbf{p}+\mathbf{q}}) - f(\varepsilon_{\mathbf{p}})}{\omega - (\varepsilon_{\mathbf{p}+\mathbf{q}} - \varepsilon_{\mathbf{p}}) + i\delta}. \quad (18)$$

Here, $f(\varepsilon_{\mathbf{p}}) = [e^{(\varepsilon_{\mathbf{p}} - \mu)/T} + 1]^{-1}$ is the usual fermi factor with the chemical potential μ and temperature T. Note also that due to the spin constraints only the combinations $2[\mathrm{Im}\chi^{\uparrow\uparrow}\,\mathrm{Im}\chi^{\uparrow\uparrow} + \mathrm{Im}\chi^{\uparrow\downarrow}\,\mathrm{Im}\chi^{\uparrow\downarrow}]$ and no mixing terms between $\uparrow\uparrow$ and $\uparrow\downarrow$ susceptibilities will enter in the intensity formula (14). The additional factor 2 results from summing over the spin.

In this weak coupling diagrammatic expansion the Coulomb repulsion parameter is understood as an effective U assuming that electronic correlations renormalize the bare onsite interaction to smaller values. $\chi^{\uparrow\uparrow}$ and $\chi^{\uparrow\downarrow}$ contain the contributions from both charge and spin fluctuations. However, the enhancement of the susceptibility near $\mathbf{Q} = (\pi, \pi)$ arises purely from the magnetic part which is responsible for the Stoner enhancement denominators while the charge fluctuations get suppressed with increasing U.

With (14)–(18) the derivation of the Raman scattering intensity from spin fluctuations is complete. Clearly, the complexity of the vertex function and the susceptibility requires a numerical evaluation. The calculations were carried out in a two step procedure: first we have determined the irreducible kernel of the dynamical spin susceptibility, i.e. the bare particle hole propagator given

in (17), and the analytic continuation of the vertex function from (15). The relevant momentum space summations were performed on discrete lattices with system size of 40×40 sites. We found this to result in an acceptable suppression of finite size effects. In all these calculations the hopping integral t was used as the energy unit and the chemical potential was fixed at $\mu = -0.3$ which is a typical value for a weak coupling one-band Hubbard model description of the high temperature superconductors for hole doping concentrations near 15% [22]. The input frequency to the vertex function was set to $\omega_i = 5.0$ which is reasonable for a typical laser frequency, if we assume a hopping energy $t \simeq 400$ meV. Having obtained the vertex function and the spin susceptibility we carried out the final momentum sum and the convolution integral over the two-spin fluctuation loop as a second step. We evaluated the convolution integral by a Riemann sum with a frequency spacing small compared to $k_B T/\hbar$. In all numerical steps a finite imaginary $i\delta$ (with $\delta \ll k_B T/\hbar$) was kept in the energy denominators to obtain a sufficiently smooth behavior of $V_{\mathbf{q}}$, $\chi(\mathbf{q}, \omega)$, and $I(\Delta\omega, T)$.

V. Results and discussion

Since the total Raman intensity is controlled by both, the spin fluctuations and the vertex function, we elucidate separately their relative influence. We focus on the role of the paramagnons first and set the Raman vertex to a constant. The spectrum obtained for $V_{\mathbf{q}} \equiv 1$ is shown in Fig. 4. It displays the Raman intensity Eq.(14) as a function of the inelastic frequency shift for various values of the Hubbard interaction U at a fixed temperature $T = 0.1$. For our convenience we divided out the Bose factor, but the inset shows the same plot with the Bose factor included. Figure 4 shows just the bare results for the diagram Fig. 1 in arbitrary units. Since even experimental data are most commonly presented in arbitrary units due to difficulties in obtaining absolute Raman intensities, we avoid here the complications of converting the results into real cross sections for photon counts or energy flux densities. This conversion which involves the multiplication of $I(\Delta\omega, T)$ with powers of the incoming and outgoing photon frequency [23], however, leaves the low frequency behavior unchanged.

Close to the AF transition the paramagnon excitations will soften in the vicinity of $\mathbf{Q}$ where most of the spectral weight is concentrated. As the momentum sum in (14) samples this region of the phase space one expects an enhancement of the low frequency spectral weight in the intensity. This explains the increasing intensity in Fig. 4 as U increases towards the magnetic instability, which for $\mu = -0.3$ occurs near $U \approx 2.4$. The similar behavior is obtained when the filling is changed by lowering the chemical potential. Since $I(\Delta\omega)/(1 + n(\Delta\omega))$ is the imaginary part of a correlation function this quantity must vanish proportional to $\Delta\omega$ (or at least with an odd power of $\Delta\omega$) for $\Delta\omega \ll 1$. The bare two-paramagnon Raman spectrum extends over the frequency scale of particle-hole excitations of twice the tight binding bandwidth. The spectrum, however, is naturally cut off by the maximum Raman frequency shift $\Delta\omega_{\max} = \omega_i$ which is equivalent to photon absorption. Finally let us point out that the lack of polarization dependence here is merely a consequence of using a constant Raman vertex function.

Figure 5 shows the influence of temperature assuming again $V_{\mathbf{q}} \equiv 1$ for a fixed value of $U = 2.35$. We find two competing effects to be relevant: first the overall intensity increases with temperature. This may seem surprising since the spin susceptibility near the wavevector

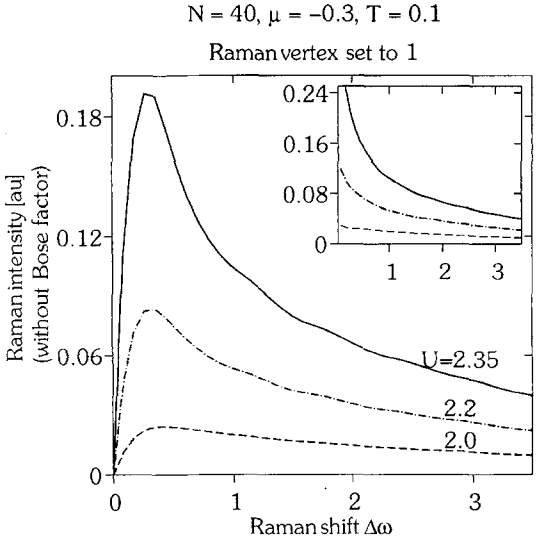

Fig. 4. Raman intensity divided by the Bose factor $1 + n(\Delta\omega)$ for fixed temperature $T = 0.1$ and different Hubbard U parameters for a constant vertex function $V_{\mathbf{q}} \equiv 1$. The inset shows the same plot with the Bose factor included. All energies are in units of the hopping matrix element t

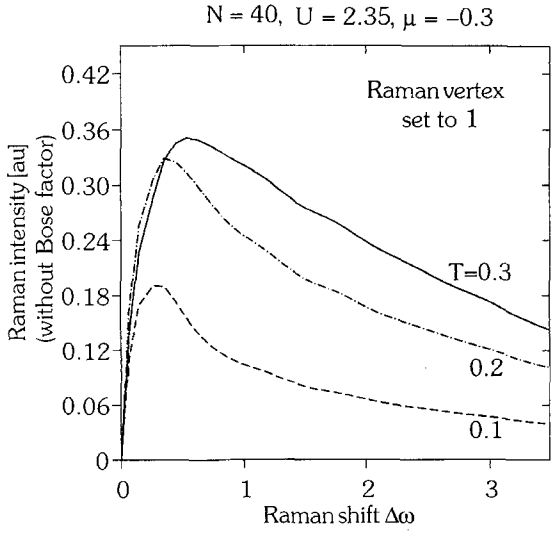

Fig. 5. Raman intensity (divided by the Bose factor as in Fig. 4) as a function of the photon frequency shift for $U = 2.35$, $\mu = -0.3$ at different temperatures for a constant vertex function $V_{\mathbf{q}} \equiv 1$

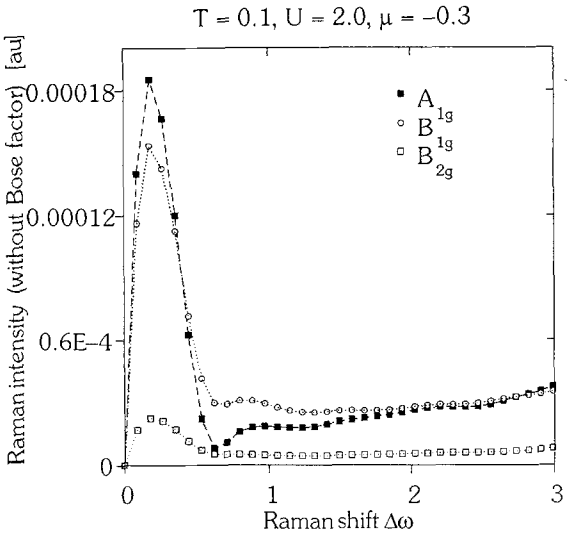

Fig. 6. Raman intensity (divided by the Bose factor) evaluated with the full vertex function for different scattering geometries of A_{1g}, B_{1g}, and B_{2g} symmetry. The dashed and dotted lines are merely a guide to the eye connecting data points of the same symmetry

$\mathbf{Q}=(\pi, \pi)$ is expected to be enhanced at low temperature. However, the $\ln {}^2T$ divergence of χ_0 at half filling is weak and cut off by a finite chemical potential away from half filling. In fact, $\mathrm{Im}\,\chi_0(\mathbf{Q}, \omega)$ increases with increasing temperature for frequencies $\omega \leqq 2|\mu|$ due to a kinematic gap in the spectral weight [24]. Here, however, the main effect arises from the temperature dependence of the Bose factor difference in the integrand of the convolution integral. Away from the very low temperature limit $T \ll \Delta\omega$ we find the convolution integrand and hence the intensity to increase with temperature due to the Bose factor difference. As a second effect the relative contribution of the low frequency peak in Fig. 5 in the spin fluctuations is enhanced as the temperature is lowered. This can be understood in terms of a quasi critical slowing down of AF paramagnons. Using a *phenomenological* form for the spin susceptibility it is exactly this concept of critical softening which has been used in [5] to describe the linear low frequency behavior of the Raman intensity.

Now we turn on the effect of the vertex function. Figure 6 shows a typical result for the total Raman intensity, including the full vertex diagrams of Fig. 2, for a fixed temperature $T=0.1$ and $U=2.0$. The three curves correspond to the polarizations of the different scattering geometries which are now distinguished by the vertex function. The differences follow from the symmetry coefficients of the vertex function listed in Table 2. The first obvious effect of $V_{\mathbf{q}}$ from this figure is the strong suppression of high frequency Raman shifts for all polarizations. This is not a trivial effect simply attributed to the high frequency falloff of the vertex. Rather this property can be traced back to destructive interference effects between the four diagrams in Fig. 2 which contribute to the vertex function. $V_{\mathbf{q}}$ is a rapidly varying function of its frequency arguments containing spikes and logarithmic singularities characteristic for the density of states of the $2d$ tight binding band. In particular the diagram Fig. 2b and its exchange counterpart Fig. 2c tend to partially cancel, nevertheless much less effective than commonly anticipated for simple metals [25] where the coupling of the light to the current is generally ignored. Figure 6 shows that with the full vertex function a pronounced scattering intensity is still maintained at low frequencies. It is this low frequency region where the spectral intensity from the scattering off the spin fluctuations is concentrated. Since the vertex function is independent of U and only weakly dependent on temperature and filling, the qualitative features discussed with respect to Figs. 4 and 5 for $V_{\mathbf{q}} \equiv 1$ will be superimposed also when the full vertex function is taken into account.

A second result which follows from this figure is the marked difference of the partial contributions of the three independent polarization geometries to the total Raman intensity. It is interesting to note that relative sizes for the A_{1g}, B_{1g}, and B_{2g} symmetries, respectively, depicted in Fig. 6 roughly correspond to the intensity ratios found in the doped cuprates. This applies in particular to the small B_{2g} contribution which is a direct consequence of the vanishing symmetry coefficient $M_\tau(\mathbf{k})$ in (15a) for the coupling to the inverse mass tensor. The slow rise of the scattering intensity as $\Delta\omega$ increases beyond the low frequeny peak is mainly due to the $1/\omega_f$ prefactor in the intensity and has no particular relevance.

VI. Conclusions

Based on the Hubbard model we have provided a microscopic analysis of Raman scattering from spin fluctuations. Our results show an increase of the low frequency scattering intensity controlled by two factors: the dynamics of spin-pair modes near $\mathbf{Q}=(\pi, \pi)$ and the high frequency behavior of the Raman vertex function. We have demonstrated the relevance of spin fluctuations on the low energy Raman cross section by varying the onsite correlation strength, i.e. the Stoner enhancement factor, and the temperature. The enhanced contribution at low frequencies is expected and consistent with the experimental observation that the two-magnon peak of the AF cuprate parent compounds broadens and moves to lower frequencies for the doped materials leaving behind a remnant low frequency feature even for the superconducting samples with a high T_c [17]. Within our approach the Raman vertex function is treated on a microscopic level. The vertex proved to be important for the spectral intensity since its nontrivial frequency dependence effectively suppresses the high energy cross section. In addition, we find the symmetry properties of the vertex function to result in intensity ratios for the different scattering geometries which are comparable with experimental findings. It is, however, unlikely that the magnetic scattering is in any way connected to the electronic background continuum. Clearly, we singled out only the dominating contribution to the magnetic Raman scattering, and other processes present in the correlated electron system may be responsible for the unusual Raman response of the cuprates. Finally, our approach also allows for an extension to the spin density wave state of

the Hubbard model at half-filling, where – besides the resonant scattering across the energy gap of the insulator [26] – itinerancy effects on the two-magnon feature may be compared to the known results for Heisenberg antiferromagnets.

The authors are grateful to J.R. Schrieffer, D.J. Scalapino, and S.C. Zhang for useful conversations. This work has been performed within the program of the Sonderforschungsbereich 341 supported by the Deutsche Forschungsgemeinschaft.

References

1. Forster, D.: Frontiers in physics. Hydrodynamic Fluctuations, Broken Symmetry, and Correlation Functions. Reading: Benjamin Cummings 1975
2. Staufer, T., Hackl, R., Müller, P.: Solid State Commun. **75**, 975 (1990); ibid. **79**, 409 (1991)
3. Slakey, F., Klein, M.V., Reznik, D., Rice, J.P., Ginsberg, D.M., Paulikas, A.P., Downey, J.W., Veal, B.W.: Proc. SPIE (Society by Photooptical Instrumentation Engineers) 1336, 1 (1990); Cooper, S.L., Klein, M.V.: Commun. Cond. Matt. Phys. **15**, 99 (1990);
   Klein, M.V., Cooper, S.L., Kotz, A.L., Liu, R., Reznik, D., Slakey, F., Lee, W.C., Ginsberg, D.M.: Physica C **185–189**, 72 (1991)
4. Varma, C.M., Littlewood, P.B., Schmitt-Rink, S., Abrahams, E., Ruckenstein, A.E.: Phys. Rev. Lett. **63**, 1996 (1989)
5. Brenig, W., Monien, H.: Solid State Commun (to be published)
6. Virosztek, A., Ruvalds, J.: Phys. Rev. Lett. **67**, 1657 (1991)
7. Sugai, S., Sato, M., Kobayashi, T., Akimitsu, J., Ito, T., Takagi, H., Uchida, S., Hosoya, S., Kajitani, T., Fukuda, T.: Phys. Rev. B **42**, 1045 (1990)
8. Singh, R.R.P., Fleury, P.A., Lyons, K.B., Sulewski, P.E.: Phys. Rev. Lett. **62**, 2736 (1989)
9. Elliott, R.J., Thorpe, M.F., Imbusch, G.F., Loudon, R., Parkinson, J.B.: Phys. Rev. Lett. **21**, 147 (1968)
10. Fleury, P.A., Guggenheim, H.J.: Phys. Rev. Lett. **24**, 1346 (1970)
11. Imbusch, G.F., Guggenheim, H.J.: Phys. Lett A **26**, 625 (1968)
12. Shastry, B.S., Shraiman, B.: Phys. Rev. Lett. **65**, 1068 (1990); Int. J. Mod. Phys. B **5**, 365 (1991)
13. Fleury, P., Loudon, R.: Phys. Rev. **166**, 514, (1968); Elliott, R.J., Loudon, R.: Phys. Lett. A **3**, 189 (1963)
14. Shirane, G., Birgeneau, R.J., Endoh, Y., Gehring, P., Kastner, M.A., Kitzazawa, K., Kojima, H., Tanaka, I., Thurston, T.R., Yamada, K.: Phys. Rev. Lett. **63**, 330 (1989)
15. Takigawa, M., Reyes, A.P., Hammel, P.C., Thompson, J.D., Heffner, R.H., Fisk, Z., Ott, K.C.: Phys. Rev. B **43**, 247 (1991)
16. Millis, A.J., Monien, H., Pines, D.: Phys. Rev. B **42**, 167 (1990)
17. Lyons, K.B., Fleury, P.A., Singh, R.R.P., Sulewski, P.E.: In: Dynamics of magnetic fluctuations in high temperature superconductors. Reiter, G., et al. (eds.). New York: Plenum Press 1991
18. Cooper, S.L., Slakey, F., Klein, M.V., Rice, J.P., Bukowski, E.D., Ginsberg, D.M.: Phys. Rev. B **38**, 11934 (1988); Slakey, F., Cooper, S.L., Klein, M.V., Rice, J.P., Ginsberg, D.M.: Phys. Rev. B **39**, 2781 (1989)
19. Kawabata, A.: J. Phys. Soc. Jpn. **30**, 68 (1971)
20. Klein, M.V.: Phys. Rev. B **24**, 4208 (1981); Klein, M.V.: In: Light scattering in solids III. Topics in Applied Physics. Vol. 51, Cardona, M., Güntherodt, G. (eds.), p. 121. Berlin, Heidelberg, New York: Springer 1982
21. Berk, N.F., Schrieffer, J.R: Phys. Rev. Lett. **17**, 433 (1966); Doniach, S., Engelsberg, S.: Phys. Rev. Lett. **17**, 750 (1966)
22. Bulut, N., Hone, D., Scalapino, D.J., Bickers, N.E.: Phys. Rev. B **41**, 1797 (1990); Phys. Rev. Lett. **64**, 2723 (1990)
23. Brenig, W.: Statistical theory of heat, nonequilibrium phenomena. Chap. 9. Berlin, Heidelberg, New York: Springer 1989
24. Bulut, N., Scalapino, D.J.: UC Santa Barbara Preprint UCSBTH-90-26 (unpublished)
25. Platzman, P.M., Wolff, P.A.: Solid State Phys. [Suppl.] **13**, 1 (1973)
26. Kampf, A.P., Brenig, W.: Ann. Phys. **1**, 206 (1992)